Chemical Engineering Journal 430 (2022) 133153

Contents lists available at ScienceDirect

Chemical Engineering Journal

journal homepage: www.elsevier.com/locate/cej

N-Graphene-Metal-Oxide(Sulfide) hybrid Nanostructures: Single-step plasma-enabled approach for energy storage applications

A. Dias [a,*], N. Bundaleska [a], E. Felizardo [a], D. Tsyganov [a], A. Almeida [b], A.M. Ferraria [c,d], A. M. Botelho do Rego [c,d], M. Abrashev [e], Th. Strunskus [f], N.M. Santhosh [g,h], U. Cvelbar [g,h], J. Zavašnik [g,h], M.F. Montemor [i], M.M. Almeida [i], Patrícia A. Carvalho [j], J. Kissovski [e], L. L. Alves [a], E. Tatarova [a,*]

[a] Instituto de Plasmas e Fusão Nuclear, Instituto Superior Técnico, Universidade de Lisboa, Av. Rovisco Pais, 1049-001 Lisboa, Portugal
[b] Centre of Physics and Engineering of Advanced Materiais, Instituto Superior Técnico, Universidade de Lisboa, AV. Rovisco Pais, 1049-001 Lisboa, Portugal
[c] BSIRG, iBB, DEQ, Instituto Superior Técnico, Universidade de Lisboa, Av. Rovisco Pais, 1049-001 Lisboa, Portugal
[d] Associate Laboratory i4HB—Institute for Health and Bioeconomy at Instituto Superior Técnico, Universidade de Lisboa, Av. Rovisco Pais, 1049-001 Lisboa, Portugal
[e] Faculty of Physics, Sofia University, 1164 Sofia, Bulgaria
[f] Institute for Materials Science, Christian Albrechts Universitaet zu Kiel, Kiel, Germany
[g] Department of Gaseous Electronics F6, Jožef Stefan Institute, Ljubljana 1000, Slovenia
[h] Jožef Stefan International Postgraduate School, Ljubljana 1000, Slovenia
[i] Centro de Química Estrutural (CQE), Departamento de Engenharia Química, Instituto Superior Técnico, Universidade de Lisboa, Av. Rovisco Pais, 1049-001 Lisboa, Portugal
[j] SINTEF Industri, Materials Physics, Forskningsveien 1, 0373 Oslo, Norway

ARTICLE INFO

Keywords:
Microwave plasmas
N-graphene
Plasma-based synthesis
Hybrid nanostructures

ABSTRACT

Hybrid graphene-based nanostructures are considered promising materials for energy storage applications. However, the synthesis of high-quality hybrid graphene nanostructures at high yields is challenging. In the present work we propose a novel, single-step microwave plasma-enabled approach to synthetize customizable hybrid graphene-based nanostructures at high-yield while preserving their quality. Hybrid N-graphene (nitrogen-doped graphene) metal-based nanostructures, for instance, can be produced at a rate of ~ 19 mg/min. The high energy density region of a microwave plasma provides sufficient energy and "building particles" fluxes towards the low-energy density plasma afterglow for the processes of assembly and growth of N-graphene sheets. Simultaneously, a controlled jet of metal-oxide(-sulfide) microparticles is sprayed into the plasma afterglow region where they bind to N-graphene sheets. Methane/methylamine are used as carbon and nitrogen precursors, combined with micron-sized MnO_2 and oxy-MnS particles to synthesize the hybrid structures. As a result, nano-sized (~10–30 nm) MnO_x particles decorated N-graphene (4.6 at. N%) and oxidized metal sulfide anchored N-graphene sheets (3.1 at. N%) are produced at atmospheric conditions. High structural quality and distribution of metal-based nanostructures on N-graphene sheets are revealed using transmission and scanning electron microscopes and other advanced spectroscopic techniques. Finally, an electrode for supercapacitor based on the N-graphene-metal-oxide(sulfide) hybrid nanostructures is developed with promising specific capacitances (~273 F. g^{-1} at 0.5 A.g^{-1}). The described chemically engineered process is one of the fastest approaches reported for designing the high-quality hybrid nanostructures produced at a high-yield, and as such, is expected to provide a high impact on the design of electrode materials for sustainable energy storage systems.

1. Introduction

Demand for high-performance electrode materials, which offer conspicuous improvement in capacitance than the existing materials for energy storage devices, has increased due to current energy production requirements. Transition metals and their varieties have been deemed as potential materials to be used as advanced electrodes for energy storage devices considering their abundance, diverse morphologies, and easy

* Corresponding authors.
E-mail addresses: ines.vieitas@tecnico.ulisboa.pt (A. Dias), elena.stefanova@tecnico.ulisboa.pt (E. Tatarova).

https://doi.org/10.1016/j.cej.2021.133153
Received 29 June 2021; Received in revised form 14 October 2021; Accepted 20 October 2021
Available online 25 October 2021
1385-8947/© 2021 The Authors. Published by Elsevier B.V. This is an open access article under the CC BY-NC-ND license (http://creativecommons.org/licenses/by-nc-nd/4.0/).

approachability. Amid the varieties of high performing transition metal derivatives, Metal oxides (MO) and Metal sulfides (MS) are gaining research interest due to their high theoretical capacitance, which could enhance the energy density of devices. Despite these advantages, low electrical conductivity, pulverization during electrochemical reactions and considerably low ion diffusion in the bulk phase have retarded their practical applications. Thus, enhancing the electrical conductivity and electrochemical stability of the transition metal derivatives is important in order to improve respective electrochemical properties.

One of the feasible approaches to address these issues is incorporating MO/MS structures into an electrochemically stable conductive matrix. In this context, graphene – the 2D carbon-based nanostructures with its unique properties, such as superior mechanical, thermal and chemical strength, extreme specific surface area, tunable surface properties, ability to withstand high temperatures and aggressive chemicals is recognized as a material of great technological interest. Graphene is widely considered one of the best electrochemically stable conductive matrices, with possible electric double layer capacitance of $\sim 550\ F{\bullet}g^{-1}$ if all the surface area of graphene can be used, which can be easily processed using different techniques [1–5]. Hence, nanocomposites of electrochemically active MO/MS structures incorporated into the graphene lattice could provide outstanding electrical and electrochemical properties. Striking advances in graphene-based nanocomposites suitable for energy storage and conversion devices have been achieved by leveraging the synergistic effects between graphene and MO/MS material. As the electrode materials in energy storage and conversion devices - either in anchored, encapsulated, sandwiched, wrapped or mixed configurations, graphene-metal oxide/sulfide-based hybrid structures have demonstrably enhanced electrochemical performance than those exhibited by each of the individual constituents. Graphene-metal oxide (GMO) composites, highlighted as a new class of advanced electrode materials, have been widely investigated in the last years. Combining the merits of graphene and MO results in new functionalities and properties. Significant synergetic effects occur in hybrid GMO composite due to the size effects and interfacial interaction [1]. In addition, MO nanoparticles attached or anchored on graphene sheets suppress agglomeration and re-stacking of the layers in the graphene sheet, serving as nanospacers and increasing the accessible surface area [2–4]. On the other hand, graphene acts as a highly conductive matrix, which can improve the electrical properties and charge transfer channels of pure oxides and restrain the volume change and agglomeration of the MOs during the charge-discharge process. Numerous nanoarchitectures of GMO-based nanocomposites with varieties of MO (SnO_2, Mn_3O_4, MnO_2, Fe_2O_3, Fe_3O_4, TiO_2, ZnO, RuO_2, etc.) were proposed, such as MO anchoring on graphene, graphene-wrapped MO particles, graphene-encapsulated MO, 2D sandwich-like structure, etc. [1,5].

More recently, MS has been considered as the next-generation prospective electrode materials due to its higher specific capacity, in some cases the double of their corresponding oxides, such as for NiS_x/NiO_x, CoS_x/CoO_x, etc. [6,7]. Even though MS is typically more conductive than MO, it still does not meet the required electrical conductivity for continuous high-performance electrochemical reactions. Also, material fragmentation during electrochemical reactions causes poor stability and reduced rate performance. Similar to the GMO composites, it has been already demonstrated that the graphene-MS (GMS) composites could address these challenges after improving the electrical conductivity and structural stability, thus enhancing the total capacitance [8]. In addition, both GMO and GMS composites give the possibility to improve their electrochemical performance by manipulating the surface defects at the nanoscale [9–11].

One of the commonly followed approaches to manipulate the structural defects in graphene is doping. Doping can also strengthen the binding forces between MO/MS nanoparticles and graphene matrix. Doped graphene possesses a modified surface charge distribution on the scaffold, with active charge sites available for nanoparticles anchoring [12–14]. Nitrogen, having higher electronegativity than carbon, is often chosen as a dopant, which can also improve the affinity of graphene towards the MO/MS anchoring [15–17]. Additionally, N-doping of graphene is also increasing the pseudocapacitive behavior of the materials by the surface redox reactions and improve the total electrochemical performance. Thus, employing N-graphene-MO (NGMO) and N-graphene-MS (NGMS) based hybrid nanostructures (hybrids) as an advanced electrode material for energy storage applications could result in a paradigm shift in sustainable energy development.

Among the varieties of MOs, MnO_2 is suggested as an ideal pseudocapacitive material due to its distinctive physicochemical properties, low-cost, abundance and environmental friendliness [1]. On the other hand, manganese sulfide groups are considered to exhibit higher conductivity than the MnO_2 and are expected to address the problem with the low electronic conductivity during the electrochemical reaction. Thus, a feasible approach for the fabrication of N-graphene-manganese oxide/sulfide hybrids is in demand for the successful application of these nanostructures for energy storage applications. Enhanced supercapacitor performances were achieved, for instance in [18], providing higher specific capacitance ($275.2\ F.g^{-1}$ at $2\ mA.cm^{-2}$, when MnO_2-N-graphene (NG) hybrid is used instead of MnO_2-graphene. A similar advancement, reported in [19], was attributed to the graphene functionalization and the uniform distribution of the MnO_2 nanoparticles. Graphene-MnO_2 composites, synthesized by redox reaction between graphene and $KMnO_4$ under microwave irradiation, have demonstrated specific capacitances as high as $310\ F{\bullet}g^{-1}$ at $2\ mV{\bullet}s^{-1}$, higher than the one of pure graphene ($104\ F{\bullet}g^{-1}$) and birnessite-type MnO_2 ($103\ F{\bullet}g^{-1}$) [20].

Despite all the advantages of NGMO and NGMS composites, one of the main challenges that needs to be solved is finding a fast and facile approach for the large-scale growth of these hybrid nanostructures. So far, the main synthesis strategies for GMO composites, i.e., *ex-situ* and *in-situ*, have led to the development of hybrids with various structures (anchored, encapsulated, wrapped, layered, mixed-structures) with improved electrochemical performances. Synthesis methods as sol-gel, hydrothermal, solvothermal, self-assembly, microwave irradiation, etc. were widely tested [5,18–27]. Hydrothermal and solvothermal are the most used approaches, where primary reduced-GO or amorphous carbon are employed [3,4]. Despite the numerous investigations and advancements in the field, the existing methods still possess several common disadvantages associated with the utilization of harsh chemistry, lengthy procedures, and, particularly, poor material quality. For instance, *in-situ* methods generally involve simultaneous chemical reduction of graphite oxide or graphene oxide and the respective MO/MS particles, typically by applying the Hummers method [28]. The produced composites suffer several problems such as moderate electrical conductivity, deficiency of micro-pores, unwanted functional groups and residue contaminants and restoration of the defects formed during the oxidation. All these factors could retard the total electrochemical energy storage performance [29]. On the other hand, pre-synthesized MS/MO hybrids are anchored on the graphene structure externally in the *ex-situ* methods. Characteristic problems of the *ex-situ* methods include the low density and non-uniform coverage of nanostructures on graphene sheets as well as the weak interfacial interaction [2,21]. Considering all these issues, there is a strong demand for a large-scale synthesis method allowing control over the graphene structural quality, i.e., level of sp^3 carbon bonds, contaminants, and bonded oxygen groups, number of layers in graphene sheet, etc. as well as size, concentration, and distribution of the MO/MS nanoparticles on graphene scaffold.

Plasma-enabled techniques circumvent the limitations of chemical-based processes and open innovative synthesis pathways. They offer a competitive alternative and sustainable strategy to synthesize disruptive complex graphene-based nanostructures by allowing an effective control over the nucleation and assembling processes at the atomic scale level, i.e., control on the entire assembly process at nanoscales [30–35]. Besides, plasma-enabled processing techniques allow the processing of

graphene-based nanostructures, either by doping or functionalization, without disrupting the structure and morphology of the carbon nanostructures. Therefore, a plasma-enabled technique that can directly produce GMO or GMS without any post-processing could overcome the issues regarding the structural quality, electrical conductivity, and structural stability. Moreover, these plasmas designed graphene-metal-based composites could be used as potential electrode materials for energy storage applications.

Herein we have demonstrated a novel single-step microwave plasma-enabled approach for the direct, continuous, and high-yield fabrication of free-standing NGMO and NGMS hybrid nanostructures at atmospheric conditions. High energy density microwave plasmas were used as a tool for supplying energy and "building particles" (C, C_2, N, CN, etc.) fluxes towards low-energy-density plasma afterglow, i.e., assembly zone of the reactor, where the processes of assembly and growth of graphene sheets with incorporated N atoms take place. Simultaneously, a controlled jet of micron-sized metal particles is sprayed from the opposite side to the assembly zone, resulting in plasma-forced size reduction of the particles and their anchoring onto growing N-graphene sheets. Hundreds of milligrams of ready for use free-standing hybrids can be fabricated in minutes (~19 mg/min). Methane and methylamine were used as carbon and nitrogen precursors for N-graphene synthesis, while MnO_2 and oxy-MnS (MnS*) micron size particles were chosen as metal oxide and sulfide precursors, respectively. The complex plasma environment was tailored to ensure the selective synthesis of N-graphene. Hybrid nanostructures of metal oxide nanoparticles attached to and wrapped with few-layered N-graphene were fabricated. A similar protocol was used to successfully obtain hybrid N-graphene-metal sulfide nanostructures. The developed technique has demonstrated the potential to ensure controllable synthesis of N-graphene with MO/MS nanoparticles intercalated between its layers, which can be used as an alternative technique for the high-yield synthesis of graphene-based nanostructures for energy storage applications.

2. Material and methods

2.1. Materials

Both metal-based powders were purchased from Sigma Aldrich: manganese dioxide activated powder, CAS 1313–13-9 (~85 %), with particle sizes < 10 μm; manganese (II) sulfide powder, CAS 18820-29-6 (~100 mesh particle size) (**Fig. S1**).

2.2. Structural and chemical characterization

The synthesized hybrid nanostructures were characterized by Scanning Electron Microscopy (SEM), High-Resolution Transmission Electron Microscopy (HRTEM), Scanning Transmission Electron Microscopy (STEM), X-ray Diffraction (XRD), Raman and X-ray photoelectron spectroscopies (XPS) and Near Edge X-ray-absorption fine-structure (NEXAFS) spectroscopy. Details regarding the experimental techniques are given in the supplementary information.

2.3. Electrochemical characterization

All the NGMS and NGMO samples were prepared using a mortar and pestle in N-Methyl-2-pyrrolidone (NMP) solvent. The resulting mixture was applied as a coating in Toray® carbon paper (Alfa Aesar) substrate (1 × 1 cm^2) and dried at 50 ℃ for 12 h in an electric oven. Electrochemical charge storage properties of the samples were evaluated in a 1 M KOH aqueous electrolyte solution, with all the values being measured versus a Standard calomel electrode (SCE).

2.4. Single-Step Plasma-Enabled approach for the N-Graphene Metal-Based hybrids

A novel microwave plasma-based method for the controllable synthesis of hybrid nanostructures, such as N-graphene-MO and N-graphene-MS hybrids, has been developed. A surface wave (SW) induced microwave plasma used as a tool for synthesis is provided by a waveguide-surfatron-based setup operating at atmospheric pressure conditions [36]. Microwave plasma is sustained by the field of travelling surface waves that simultaneously propagate and create their own propagation structure, thus creating an extended active zone outside the wave launcher (Fig. 1). As a result, large microwave power densities can be inserted into the processing area and high population densities of active species of interest can be attained. 2 kW of microwave power at 2.45 GHz is provided by a microwave generator connected to a waveguide system. The waveguide system includes a water-cooled circulator, a three-stub tuner, a moveable short-circuit and a waveguide-surfatron as the wave-launcher. A quartz reactor with a special geometry containing a section with expanding radius is inserted perpendicularly to the waveguide wider wall and directed downstream. The quartz reactor comprises two sections: a small one with internal and external radii of 0.75 cm and 0.9 cm, respectively, connected via conical section to the large tube with internal and external radii of 2.15 cm and 2.3 cm, respectively. The design permits control over the thermodynamics and kinetics of the system, i.e., important parameters such as gas velocity, energy fluxes, residence time, etc. can be adjusted [37,38].

The plasma driven processes of N-graphene sheet formation starts with the decomposition of carbon and nitrogen precursors in the "hot" plasma medium (Fig. 1), as a result of collisions with electrons and heavy particles and intense radicals' chemistry [34,36,39,40]. The created gas-phase carbon atoms, C_2 and N-containing radicals are transferred towards colder zones of the plasma through the so-called surface of vaporization (separating the "hot" from the "mild" plasma zone in Fig. 1), leading to their conversion into solid nuclei. The kinetic processes of assembly and growth of N-graphene sheets occur in the "mild", i.e., "assembly" plasma zone, during their flow with the background Ar gas. The engineering of structural qualities of targeted nanostructures was achieved via synergistic tailoring of the conditions in the "hot" and the assembly plasma zones, i.e., by managing the temperature gradients, the number density of carbon and nitrogen atoms and radicals, as well as the residence time in the assembly zone of the plasma reactor (Fig. 1). Moreover, the control on the type of nitrogen-containing species and their densities in the "hot" plasma zone, results in control on the doping level, type of N bonding configurations, and N-graphene production yield (Fig. 1). The plasma parameters were kept the same for both hybrid nanostructures, background argon flow of 1200 sccm, methane flow of 20 sccm and methylamine flow of 6 sccm.

Furthermore, while the N-graphene sheets are being assembled in the upper part of the "assembly zone", a controlled flow of microparticles (MnO_2 or oxy-MnS) is sprayed upstream into the reactive plasma medium. For NGMO synthesis MnO_2 flow was 1.4 g/h, while NGMS were produced with oxy-MnS (MnS*) flow of 0.3 g/h. The microparticles, placed in a specially designed injector system, are carried by an optimized argon flow (~300 sccm), and sprayed in an appointed position in the "mild" plasma zone of the reactor. The microparticles when injected rapidly heat up to the temperature of the background gas, which is around 2000 K in the insertion zone. Here the micron-sized particles undergo plasma forced size reduction and are converted into nanoparticles. Moreover, they are involved in a plasma-activated chemical reaction with radicals, atoms, and molecules (H_2, C, CN, HCN, etc.), resulting in the formation of different phases and their anchoring to the growing N-graphene sheets (Fig. 1).

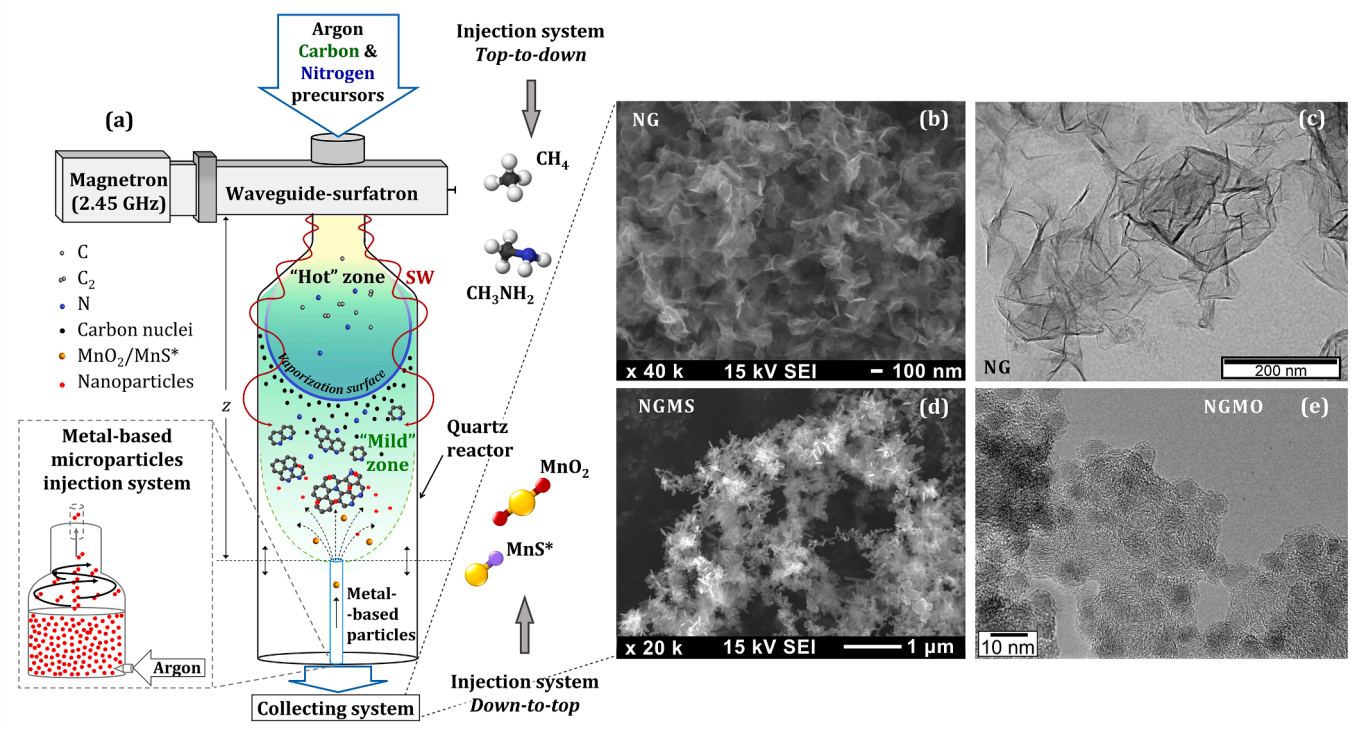

Fig. 1. (a) Schematic representation of the experimental setup. (b) SEM and (c) TEM micrographs of NG sheets. (d) SEM micrograph of NGMS. (e) TEM micrograph of NGMO.

3. Results and discussion

3.1. Characterization of N-Graphene-Manganese oxide (NGMO) hybrid nanostructures

Understanding the surface and structural characteristics of the synthesized nanostructures is crucial for application-oriented purposes. Thus, the surface and structural organization of the nanostructures are investigated by TEM analysis. The formation of graphene-like sheets and particle-like structures can be easily identified in the TEM image of the assembled NGMO nanostructures, suggesting that manganese oxide nanoparticles are present together with N-graphene sheets (Fig. 2). Free-standing N-graphene sheets exhibit typical curled graphene morphology [34–36]. Folded and entangled thin wavy sheets can be seen as transparent zones and dark lines due to the folding up of the sheet edges (Fig. 2**a, b**). HRTEM analysis indicates the presence of nanoparticles dispersed in the matrix of N-graphene sheets. Nanoparticles possess different morphologies with different size distribution (<100 nm). Some particles are nearly spherical, while others are elongated or squared and present faceted interfaces (Fig. 2**a, b**). Even though, nanoparticles formed with different sizes, the average size of particles is in the range of 5–30 nm (Fig. 2**c, e** and **Fig. S2**).

Selected area electron diffraction (SAED) analysis along with the corresponding Fast Fourier Transform (FFT) patterns show the presence of N-graphene and MnO nanoparticles as the major phases, together with some particles corresponding to the α-Mn_3O_4 phase (Fig. 2**d, e**). No sign of the original MnO_2 was detected as evidenced by XRD analysis (Fig. 2**f** and **Fig. S1**). The XRD pattern reveals several peaks indicating the presence of different nanocrystalline phases. It shows not only the N-graphene typical peaks (signed by NG in Fig. 2**f**), but also intense peaks indexed as the cubic $Fm\bar{3}m$ MnO phase (PDF#07–0230), $a = 0.4445$ nm. Minor diffraction peaks marked by blue spots in the diffractogram can be attributed to the tetragonal α-Mn_3O_4 phase, I41/amd (PDF #24–0734). The average crystalline size was estimated using Scherrer's equation. The values obtained for the oxide nanoparticles are 25–30 nm and 22 nm for MnO and α-Mn_3O_4, respectively. The N-graphene interlayer spacing measured from HRTEM images provides a value of 3.54 ± 0.07 Å, which is in line with the d-spacing calculated from the d_{002} diffraction line position (Fig. 2**d-f**).

The results clearly demonstrate the formation of new phases and thermally driven particle size reduction during the plasma synthesis process. Two typical architectures can be easily identified, i.e., attached MO nanoparticles to the N-graphene and between sheets, and MO nanoparticles wrapped with the sheet (Fig. 2 **(a–c)**). Following the thermodynamic analysis performed (**Fig. S3**), MnO_2 particles with a diameter < 10 μm sprayed in the plasma medium will quickly heat up to the temperature of the carrier gas considering convective and radiative heat transfers between the particles and the plasma flow. The temperature of the particles practically follows that of the carrier gas, with the maximum deviation ~ 50 K under the conditions considered. Introducing the MnO_2 microparticles into the "mild" plasma zone will result in their heating up to ~ 1600–1700 K (the gas temperature corresponding to the injection location), followed by the respective reduction in the C-rich environment into lower oxidation state compounds (Fig. 3**a (1)-(2)**) [41]:

$$MnO_2 \xrightarrow{873K} Mn_2O_3 \xrightarrow{1223K} Mn_3O_4 \xrightarrow{1573K} MnO$$

The release of oxygen results from its diffusion towards the surface via micropores and microcracks of the microparticle. The newly transformed MnO particles in the "mild" plasma zone undergo a diffusion flow of the plasma species (H_2, C, HCN, etc.) towards the surface [42]. At the MnO surface and the subsurface region, these active plasma species cross the path of oxygen species previously released from MnO_2 precursor and reactions between them take place:

$$O_2 + 2H_2 \xrightarrow{surface} 2H_2O$$
$$2C + O_2 \xrightarrow{surface} 2CO$$
$$2CO + O_2 \xrightarrow{surface} 2CO_2$$

Furthermore, the species H_2O, CO, and CO_2 will leave the surface of

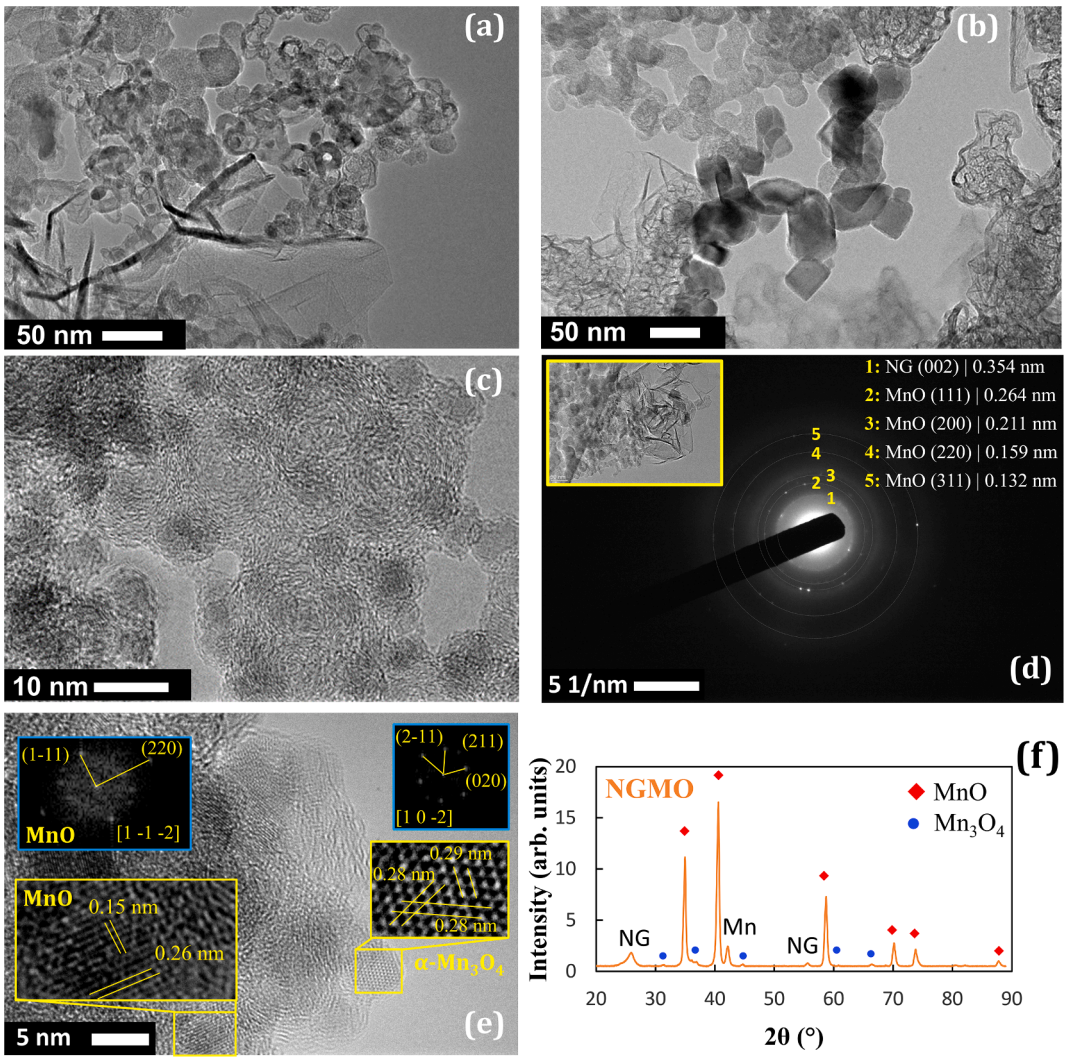

Fig. 2. Surface and structural characteristics of NGMO hybrids: (a) (b) TEM, (c) HRTEM, (d) SAED, (e) HRTEM image with FFT analysis, and (f) XRD pattern.

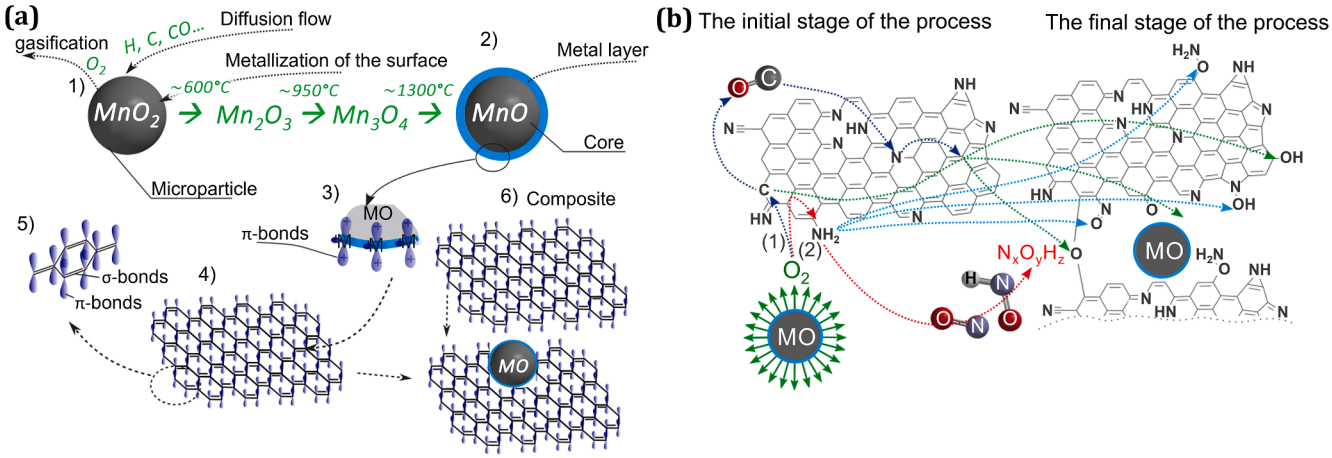

Fig. 3. (a) Schematic representation of NGMO hybrids formation in the plasma environment: (1) initial MO transformation, (2) final MO phase, (3) π* metal complexes, unfilled (electron-acceptor) orbitals of the metal surface atoms, (4) NG monolayer, (5) π–π* interactions in the hexagonal rings of NG monolayer, (6) the final NGMO hybrid nanostructure; (b) Schematic representation of oxygen interaction with N-graphene monolayer ((1) and (2)- possible channels).

the particles. Since CO and CO_2 formed in these processes are very small fractions of the total concentration of gaseous carbon present in the plasma volume, the water and CO_2 will continue to react with carbon [42]:

$$CO_2 + C \rightarrow 2CO$$

$H_2O + C \rightarrow CO + H_2$

Due to the limited size of the nanoparticles, the total diffusion of oxygen flow to the surface will decrease with time. After the total oxygen flow becomes less than the total H_2 and C flow towards the surface, the latter will be adsorbed on the surface of the MnO:

$C(gas) \rightarrow C(adsorption)$

$H_2(gas) \rightarrow H_2(adsorption)$

The H_2 and the C are known as good reducing agents; thus, the reduction of MnO to Mn can occur, starting from the surface of the nanoparticle [41]:

$MnO(surface) + H_2(adsorption) \rightarrow H_2O + Mn(surface)$

$MnO(surface) + C(adsorption) \rightarrow CO + Mn(surface)$

Based on this reduction process, the micro-sized MnO particles are reduced into nanoparticles with a metallic outer layer (Fig. 3**a (1)–(6)**).

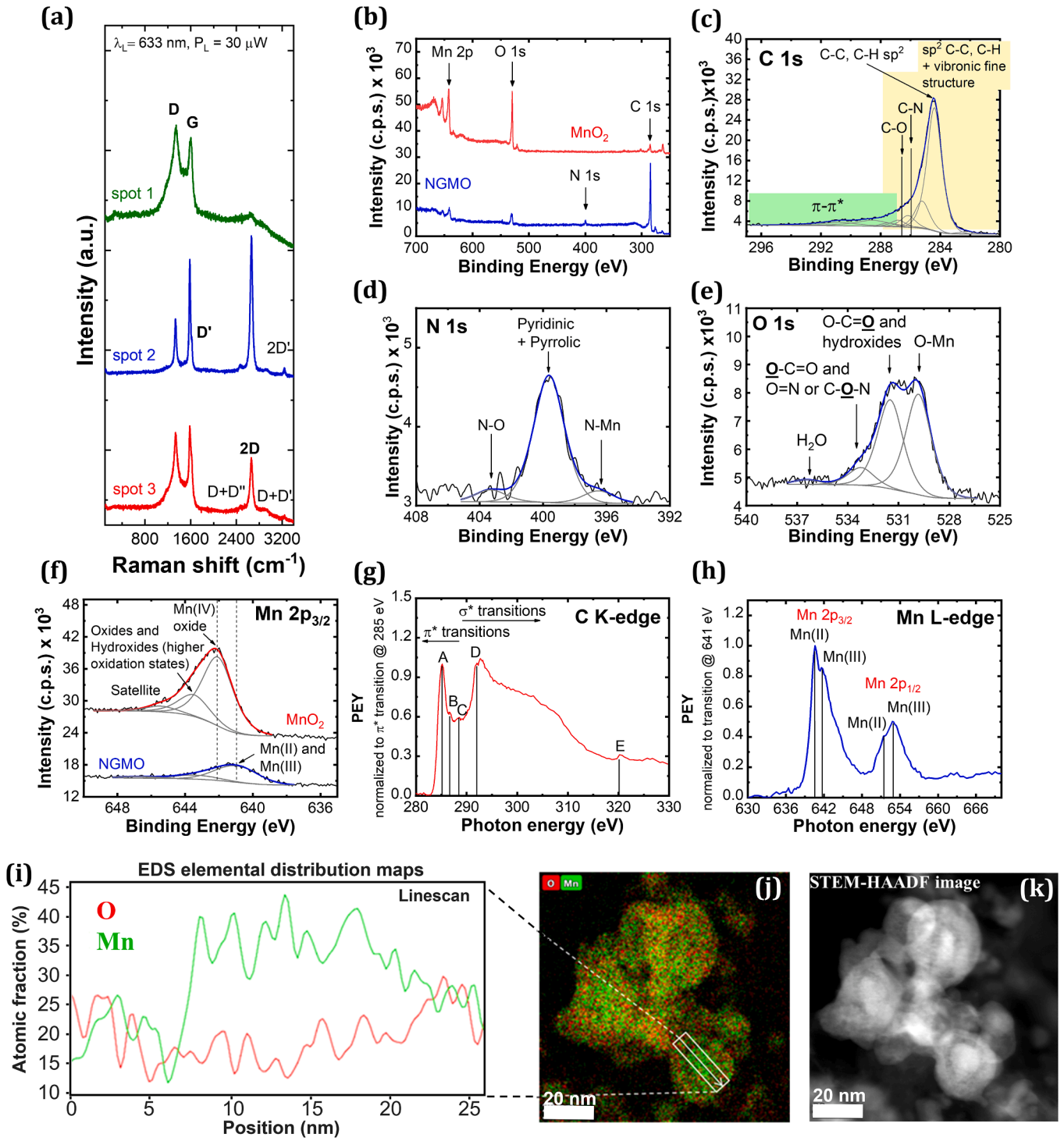

Fig. 4. (a) Raman spectra at three random locations of the NGMO sample. (b-f) XPS spectra: (b) survey of NGMO and injected MnO_2 microparticles, (c) C 1s, (d) N 1s, (e) O 1s and (f) Mn 2p spectral lines of NGMO hybrids. (g) C K-edge and (h) Mn L-edge spectra of the NGMO hybrids, (i-j) EDS mapping and line-scan of the elemental distribution of Mn (green) and O (red) and respective (k) STEM-HAADF image of the NGMO hybrids.

Islets of a thin metal Mn layer around the particle surface facilitate its attachment to the N-graphene sheets, due to the higher reactivity of Mn. If a nanoparticle captured by a free-standing N-graphene monolayer does not rotate or slightly rotates around the bond axis, another N-graphene monolayer can attach to it due to the weak van der Waals force, electrostatic force, or π-π* interactions. If the rotation energy relative to the deformation energy of the NG monolayer is large, then wrapping of the monolayer around the nanoparticle can take place, as observed by HRTEM (Fig. 2**c**). As a consequence, the wrapping of the N-graphene monolayer around the nanoparticle will shield the flow of H_2 and C species. Thus, the compensation mechanism stops to work, and the nanoparticle becomes a point source of oxygen (Fig. 3**b**). Due to the proximity of the source to the N-graphene monolayer the released oxygen begins to interact with the N-graphene structure. Two possible channels of oxygen interaction with the N-graphene monolayer are proposed: the first (Fig. 3**b (1)**) is a simple attachment of oxygen to the N-graphene lattice, creating different oxygen groups (bulk and edge), which will increase the total concentration of oxygen atoms in the N-graphene structure. Further, detachment of carbon atoms from the N-graphene monolayer can occur, leading to the formation of CO. However, the nitrogen atoms in the N-graphene monolayer act as negative vacancy (NV^-) centers. The interaction brings the carbon atom from CO molecule (slightly positive), at a critical distance to the N-graphene structure (NV^- center) resulting in a covalent bonding with the lattice structure (Fig. 3**b**), forming different oxygen groups [37]. The second possibility (Fig. 3**b (2)**) of the oxygen incorporation in the N-graphene scaffold will lead to its interaction with various cyano-groups: R-C-NH_2, R-C = NH, R = C = NH, R-C-O-NH_2, R-N = O, etc. As a result, the cyano-groups will transform into various nitrogen oxides NxOyHz, the latter can leave the N-graphene surface, thus reducing the nitrogen concentration in NGMO (Fig. 3**b (2)**).

In order to identify the structural quality and chemical composition of prepared NGMOs, different surface analyzing spectroscopy techniques were employed. The Raman spectra, obtained from three different randomly chosen spots of the NGMO samples, are shown in Fig. 4**a**. The three main peaks, attributed to D, G, and 2D-bands typical for the graphene-like materials are present, although in the first spectrum (spot 1) the 2D peak is not as sharp and intense as the ones from the other two spectra (spots 2 and 3). The G peak, originating from in-plane vibrations, appears in all sp^2 carbon systems. The intensity and shape of the 2D peak, which corresponds to the overtone of the D band, are very sensitive to the number and the stacking order of graphene sheets [43]. The intensity ratio between the 2D and G peaks and the full width at half maximum (FWHM) of 2D peak indicates that both few-layered (e.g., FWHM ~ 26 cm^{-1}, I_{2D}/I_G ~ 0.73) and multi-layered (e.g., ~34 cm^{-1}, I_{2D}/I_G ~ 0.44) graphene sheets are present in the NGMO hybrids [41,43]. The intensity of D and D' (small shoulder of G) peaks depend on the type of defects and their concentration in the graphene layer and the size of graphene flakes. The presence of nanoparticles and the doped nitrogen atoms in the sample represent structural defects in N-graphene, contributing to the D band intensity. The spectra detected at different randomly chosen locations of the sample differ, implying its inhomogeneity. The inhomogeneity is expected, since nanoparticles are attached to and between the sheets. This result is in accordance with HRTEM observations. The low-intensity peak detected at ~ 275 cm^{-1} can be attributed to the atomic vibrations of the metal oxides. (Note: the most intense lines in the Raman spectra of alpha-MnO_2 are in the 500–700 cm^{-1} region) [44,45].

The XPS survey spectrum of the synthesized hybrid nanostructure reveals the presence of carbon, nitrogen, oxygen, and manganese (Fig. 4**b**). Additionally, the XPS analysis of the reference MnO_2 powder was performed (Fig. 4**b**). The contributions to C 1s, N 1s, O 1s and Mn $2p_{3/2}$ photoelectron regions and their assignments can be seen in Fig. 4**c–f**. The shape of the C 1s photoelectron line and its fitting contributions (Fig. 4**c**) show two main features typical of an aromatic system, i.e., the dominant peak center at 284.4 eV attributed to sp^2 C–C and/or C–H and a wide hump in the range 287 eV – 295 eV corresponding to energy losses due to π-π* electronic excitations. Carbon atoms bonded to nitrogen or to oxygen are included in the peaks center at 286.2 eV and 286.8 eV, respectively. The N 1s region was fitted with three peaks (Fig. 4**d**). The dominant peak, center at 399.6 ± 0.1 eV, is assigned to a mixture of pyridinic and pyrrolic nitrogen, which are typically found at 399.3 eV and 399.9 eV, respectively. The peak at lower binding energies, center at ~ 396.5 eV, can be assigned to nitrogen atoms bonded to a metal (an electropositive atom), like Mn, while the peak around 403 eV typically originates from N—O bonds. The main peak in the O 1s region (Fig. 4**e**) of the NGMO hybrid is center at 529.8 ± 0.1 eV is attributed to O—Mn bonds, whose analogue in MnO_2 pristine powder is found at 529.7 ± 0.1 eV. However, the dominant peak in Mn $2p_{3/2}$ region (Fig. 4**f**) of MnO_2 powder center at 642.1 eV, for NGMO is found at 641.0 ± 0.1 eV, i.e., it is shifted towards lower binding energies (*Cf.* assignments in Table 1). This shift indicates a reduction of MnO_2, due to the plasma process. The quantification (Table 1) shows relatively high nitrogen doping level ~ 4.6 at. % N, as well as indications that the stoichiometry of the metal oxide has changed: for the injected MnO_2 microparticles the atomic ratio $O_{529.7}$/Mn is ~ 1.8, while for the NGMO hybrids $O_{529.8}$/Mn ~ 1.3. Hence, new phases such as Mn(II) and Mn(III) are formed due to the reduction reaction, as already proved by XRD and HRTEM/SAED results. (Note: O/Mn corresponds to the ratio between the atomic concentrations of oxygen bonded to manganese and manganese, see Table 1)

The nature of chemical intra-molecular bonding of the NGMO hybrid nanostructure has further been analyzed by NEXAFS. The C K-edge NEXAFS spectrum (Fig. 4**g**) in the partial electron yield mode (PEY), reveals a characteristic sharp C 1s → π* resonance at ~ 285.2 eV (region A) and σ* resonance at ~ 292 eV (region D), where π* and σ* refer to the anti-bonding molecular orbitals. Higher energy peaks result from transitions towards higher-lying states of π or σ symmetry. Features, observed in the region 286–290 eV, are typically attributed to the presence of impurities in the graphene lattice, including doping. The residual peak observed at ~ 286.7 eV (region B) is attributed to C═N bond and the one at ~ 288.3 eV (region C) to O—C═O bond. The peak identified at ~ 320.1 eV (region E) is usually attributed to Mn-O. Furthermore, Mn L-edge NEXAFS spectrum shows two distinct transitions, i.e., $2p_{3/2}$ and $2p_{1/2}$, which can be deconvoluted in two contributions that are frequently attributed to two oxidation states of manganese, namely Mn(II) and Mn(III) [49,50], in accordance with XPS and HRTEM analysis made.

Additionally, high-angle annular dark-field (HAADF) and elemental mapping analysis were performed using a Scanning Transmission Electron Microscope (STEM) with a Super-X energy dispersive X-ray (EDS) detector. The HAADF image and EDS map (Fig. 4**i–k)** show agglomeration of structures at different degrees of crystallinity and different oxidation states, as already demonstrated by XPS and NEXAFS analysis. The performed line-scanning indicates that the region of interest has more manganese than oxygen at the center and equal amount of both elements at the edges, i.e., different oxidation states.

3.2. Characterization of N-Graphene-Manganese sulfide (NGMS) hybrid nanostructures

SEM and TEM micrographs of the fabricated N-graphene-manganese sulfide hybrid nanostructures, shown in Fig. 5**a, b**, demonstrate graphene-like sheets decorated with nanoparticles of different sizes, ranging from few to 150 nm.

X-ray diffraction pattern and XPS analyses of both the synthesized NGMS hybrid and the original MnS* powder were performed (Fig. 5 and 6 and **Fig. S1**). It should be noted that XRD and XPS results indicate the presence of oxygen in MnS* powder used as starting material (Fig. 5 and 6 and **Fig. S1**). The X-ray diffractogram, presented in Fig. 5**c**, shows several well-defined peaks, indicating the presence of crystalline phases, indexed as MnS, MnO, $MnSO_4$ (PDF#29–0898) and $MnSO_3$

Table 1
Corrected Binding Energies (BE) (eV) ± 0.1 eV and corresponding assignments of fitted peaks for the NGMO and MnO_2 microparticles, which were injected in the plasma reactor (as reference); Atomic concentrations (%) and relevant atomic ratios.

	BE (eV) NGMO	MnO2 (reference)	Assignments [46–48]	At. Conc. (%) NGMO		MnO2 (reference)
C 1s	284.4		C–C and/or C–H sp^2	**C**	82.2	25.3
	285.2	285.0	C–C and/or C–H sp^3			
	286.2		C-N in NGMO, mainly C 1s vibronic structure			
	286.8	287.0	C-O (residual in NGMO), mainly C 1s vibronic structure in NGMO			
	287.5		Mainly π-π*			
	288.5	289.0	Mainly π-π* in NGMO; O-C = O, (residual in NGMO)			
	290–295		π-π*			
O 1s	529.8	529.7	***O***-Mn	**O**	9.8	53.3
	531.5	531.4	O-C = ***O*** (with C-aromatic in NGMO); Mn hydroxides			
	533.2	532.8	***O***-C = O (or ***O*** = N- or C-***O***-N in NGMO)			
	536.5	534.7	H_2***O***			
N 1s	396.5		***N***-Mn	**N**	4.6	—
	399.6		Pyridinic (399.3) + Pyrrolic (399.9)			
	403.3		***N***-O			
Mn $2p_{3/2}$	641.0		Mn(II) and Mn(III)	**Mn**	3.5	21.4
		642.1	Mn(IV)			
	643.3	643.5	Mixture of Mn(IV) and other oxides or hydroxides; Mn with higher oxidation states			
	646.8	645.4	Satellites			
Atomic ratios						
			NGMO			**MnO_2 (reference)**
C/Mn			23.6			1.2
$O_{"O-Mn"}$/Mn			1.3			1.8

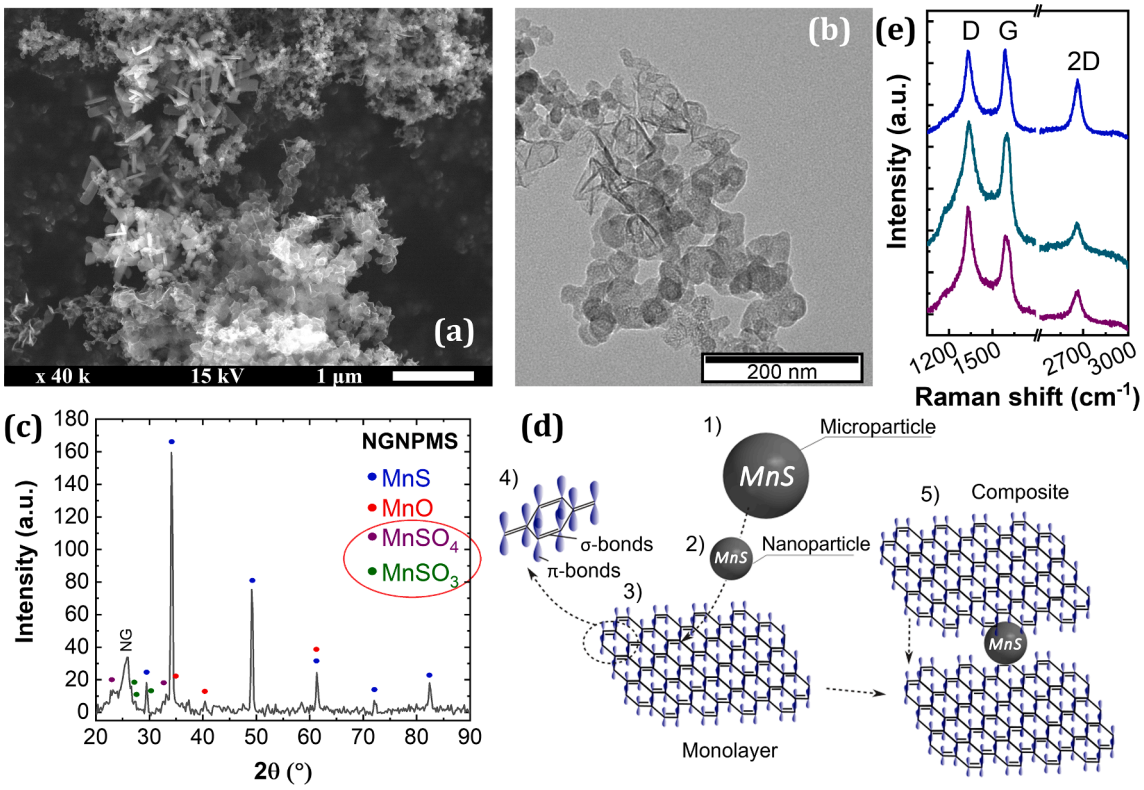

Fig. 5. (a) SEM, (b) TEM, (c) XRD of the NGMS hybrids, (d) schematic representation of the free-standing NG (monolayer) decoration process with MS nanoparticles in the plasma: 1) MS particle injection, 2) MS Nanoparticle, 3) NG, 4) π–π* interactions in the hexagonal rings of NG monolayer, 5) the final NGMS hybrid nanostructure, and (e) Raman spectra of the NGMS hybrids.

(PDF#31–0837). The N-graphene features are also present. Comparing the diffraction patterns of NGMS and the original MnS, it can be seen that (Fig. 5**c** and **Fig. S1**), the new structures created during the plasma process are MnO, with a possible minor contribution of $MnSO_4$ and $MnSO_3$.

Following the similarity in the temperature behavior of MnS and MnO_2, the Metal sulfide (MS) microparticles sprayed in the plasma medium will rapidly heat up to the temperature of the carrier gas. Due to

the presence of oxygen in the as injected MnS powder, the oxidation process takes place. Two hypotheses related to the primary products of sulfide oxidation exist, i.e., sulphate and oxide. Considering oxide hypothesis, the MnS oxidation process advances according to the scheme: $2MnS + 3O_2 \rightarrow 2MnO + 2\,SO_2$, $SO_2 + 1/2O_2 \rightarrow SO_3$, $MnO + SO_3 \rightarrow MnSO_4$.

Considering the sulphate hypothesis, the primary product of metal sulfide oxidation is a metal sulphate: $MnS + 2O_2 \rightarrow MnSO_4$, while metal oxide is formed as a result of secondary reactions, such as thermal dissociation of the sulfate: $MnSO_4 \rightarrow MnO + SO_3$, and as a result of the interaction of primary sulphate with sulfide: $MnS + 3MnSO_4 \rightarrow 4MnO + 4SO_2$, $MnS + MnSO_4 \rightarrow 2Mn + 2SO_2$. As in the case of MnO, a diffusion flow of the plasma species (H_2, C, HCN, etc.) towards the surface of the MS microparticle will appear. However, in the present case, the partial metallization of the MS nanoparticle cannot be expected [41]. The latter indicates absence of 'free' π - orbitals of the surface atoms. Therefore, the interaction between the MS nanoparticle and the N-graphene sheet becomes possible only via weak van der Waals forces or electrostatic forces (Fig. 5**d**).

The presented Raman spectra are collected over three random locations of NGMS sample (Fig. 5**e**). All spectra contain the typical features of N-graphene, i.e., D, G and 2D peaks. The existence of 2D peak indicates the graphene nature of the samples. The increase of the D peak intensity in two of the spectra (cyan and purple) implies enhanced concentration of defects, that could also be due to the incorporated nitrogen atoms in the graphene scaffold.

The survey XPS spectra and the detailed C 1s, N 1s, O 1s, Mn $2p_{3/2}$ and S 2p regions of the synthesized NGMS hybrids and of the MnS* powder, used as a reference, are presented in Fig. 6. The expected peaks for each sample are clearly detected in the survey spectra. Additionally,

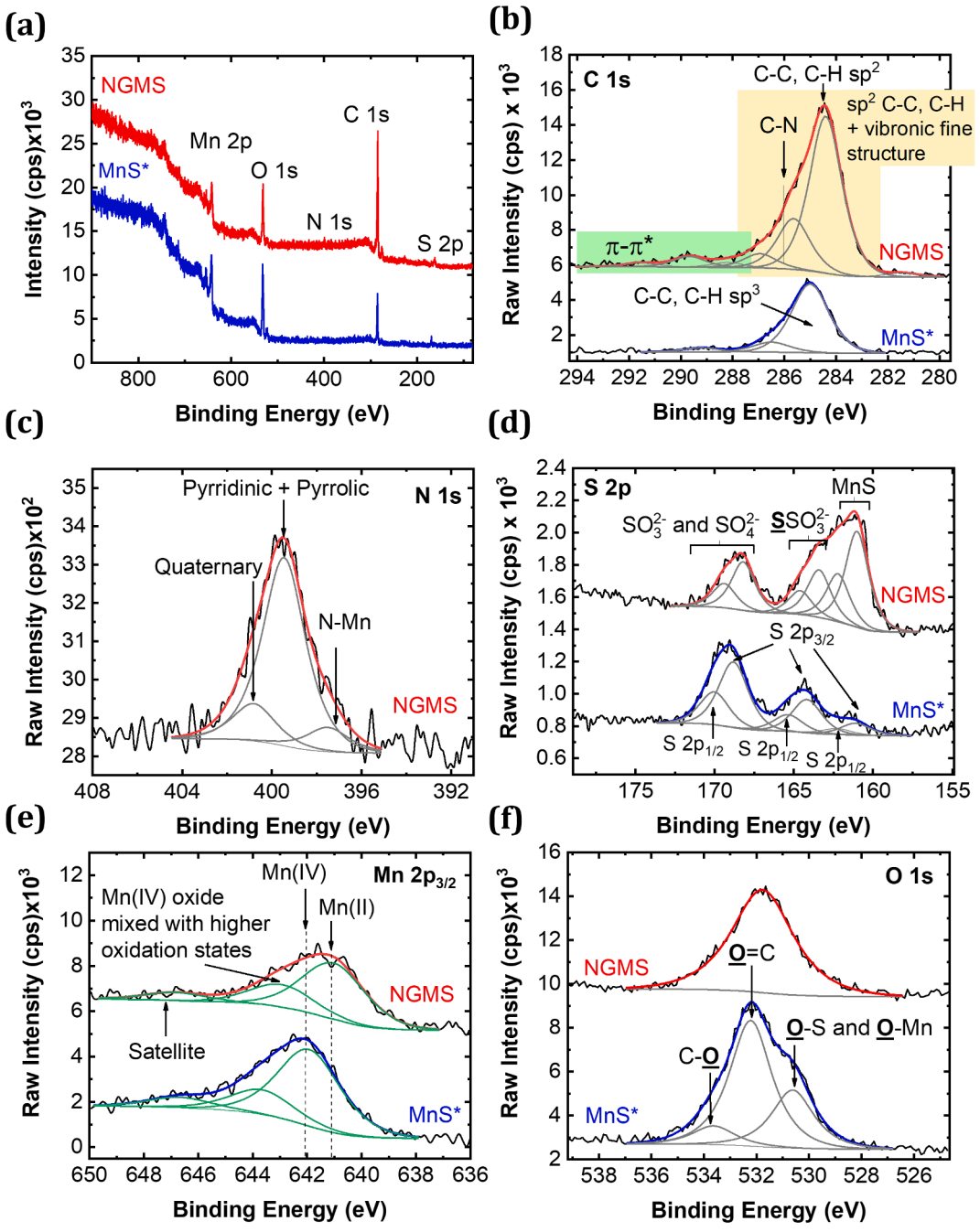

Fig. 6. XPS spectra of the original MnS* and the NGMS hybrids: (a) Surveys, (b) C 1s, (c) N 1s, (d) S 2p, (e) Mn 2p and (f) O 1s.

intense peaks assigned to O 1s are detected in both samples, and some carbonaceous contamination is also present in the reference MnS* powder (Fig. 6**a**). Fig. 6**b** shows the detail of the C 1s regions: while in NGMS the dominant peak is assigned to sp^2 carbon atoms, as expected for graphene, in MnS*, the most intense feature comes from sp^3 carbon (*Cf.* complete assignment in Table 2). In N 1s region, the dominant peak, center at ~ 399.5 eV, and the one center at lower binding energies, at ~ 397.5 eV, have the same assignments as those of NGMO N 1s. For the peak at a higher energy, a mixture of pyridinic and pyrrolic nitrogen bonding configurations, and for the one at lower energies nitrogen atoms bonded to a metal (an electropositive atom) (Fig. 6**c**). The peak center at ~ 400.8 eV is attributed to quaternary nitrogen. The nitrogen doping level achieved was ~ 3.1 at. %N (Table 2). The detailed S 2p regions reveal undoubtedly that the MnS, used as original injected powder, is in fact manganese sulfide mixed with manganese sulfonate and sulphate species (for that reason the starting powder is being labelled here "MnS*") (Fig. 6**d**).

The S 2p region of MnS* was fitted with a minimum of 3 doublets, with S $2p_{3/2}$ components center at 161.1 ± 0.1 eV, 164.2 ± 0.1 eV and 168.8 ± 0.1 eV, assigned to manganese sulfide (S^{2-}), thiosulfonate ($\underline{S}SO_3^{2-}$) and a mixture of sulfonate with sulphate species (SO_3^{2-} and SO_4^{2-}), respectively (*Cf.* complete assignment in Table 2). The S 2p spectrum of NGMS clearly shows a decrease in the relative amount of oxidized species present in the sample, namely SO_4^{2-} and SO_3^{2-}. Comparing with the original injected powder (MnS*), the fraction of oxidized sulphur species in NGMS is nearly half the fraction existing in MnS*: $S_{oxidized}/S_{Total}$ is equal to 0.5 in NGMS against 0.9 in MnS* (**Fig. S3** shows the difference between the NGMS and the MnS* S 2p spectra). Thus, the plasma environment, i.e., mild and afterglow regions, promotes the decrease in the amount of oxygen present in the synthesized nanostructures. Regarding the Mn $2p_{3/2}$ region, in the MnS* reference powder, the main peak is center at 641.9 eV ± 0.1 eV, shifting to lower BE (641.0 ± 0.1 eV) for the NGMS sample (Fig. 6**e**). This shift indicates a reduction of Mn oxidation state, from mainly Mn(IV) in MnS* (i.e., in the original oxy-manganese sulfide particles) to mainly Mn(II) in the NGMS sample, confirming what is observed in S 2p (*Cf.* complete assignments in Table 2). Finally, O 1s regions (Fig. 6**f**) include the oxygen from the oxidized species identified and described above and in Table 2. O 1s from the reference MnS* powder was fitted with 3 peaks, center at 530.6 ± 0.1 eV, 532.2 ± 0.1 eV and 533.6 ± 0.1 eV. The peak center at lower BE corresponds mainly to oxygen bonded to sulphur in sulphate groups and most probably to oxygen bonded to Mn (typically detected at 529.7 eV in MnO_2 (Table 2)). Peaks center at higher BE are mostly attributed to C = $\underline{O}$ (~532 eV) and $\underline{O}$-C (~533.6 eV). NGMS presents a symmetric, although large O 1s peak (full width at half maximum $(fwhm)_{(NGMS)} = 2.7$ eV, while $fwhm_{(MnS^*)} = 1.9$ eV), which includes all the contributions described above.

3.3. Electrochemical characterization of NGMO and NGMS hybrids

The electrochemical performance of the synthesized NG, NGMO and NGMS hybrids in the 1 M KOH electrolyte was investigated. The leaf-shaped voltammogram in Fig. 7**a** for NGMS evidence its resistive behavior under cycling. Moreover, for this hybrid nanostructure both cathodic and anodic branches reveal poor reversibility as the scan rate increases (plots not shown). Although NGMS achieves higher specific capacitance values than NGMO, its capacitance retention is quite low (Fig. 7**b**), reaching only 25.6% when the current increases from 1 to 10 $A.g^{-1}$. However, the capacitance retention of NGMO is, 76.3% which can be considered very good for Mn-based hybrid materials. Both hybrids delivered significantly higher capacitance compared to NG. NG exhibited impressive constant capacity retention of nearly 100% after 5000 cycles (Fig. 7**c**). NGMO performs very well after a long-term stability test, retaining 88% of specific capacitance after 4000 cycles (Fig. 7**c**). NGMS showed a decrease of around 53% after 200 cycles, remaining stable around this value after 5000 cycles (Fig. 7**c**).

With an active potential window of 0.55 V, NGMO shows a nearly rectangular shaped voltammogram where very attenuated waves can be observed, pointing out the pseudocapacitive nature of the hybrid nanostructure (Fig. 7**a**). Also, the voltammogram shape is retained both in the cathodic and anodic sweeps at slow and fast scan rates (Fig. 8**a**). These features are a clear indication of the excellent reversibility of the material. The galvanic charge discharge (GCD) measurements, performed at various charge densities, from 0.5 to 10 $A.g^{-1}$, evidence a linear charge-discharge profile (Fig. 8**b**), confirming the pseudocapacitive electrochemical response of the material. As expected, the

Table 2
Corrected Binding Energies (BE) (eV) ± 0.1 eV and corresponding assignments of fitted peaks for the NGMS and MnS* microparticles, which were injected in the plasma reactor (as reference); Atomic concentrations (%) and relevant atomic ratios.

	BE (eV)		Assignments [46–48]	At. Conc. (%)		
	NGMS	MnS*(reference)			NGMS	MnS*(reference)
C 1s	284.4		C–C and/or C–H sp^2	**C**	67.4	41.2
	285.6	285.0	C–C and/or C–H sp^3;also includes C-N in MGMS			
	286.9	286.5	C-O; mainly C 1s vibronic structure in NGMS			
	288.2		C = O (residual)			
		289.2	O-C = O			
	290–292		π-π*			
O 1s		530.6	$\underline{O}$-S and $\underline{O}$-Mn	**O**	19.0	41.5
	531.8	532.2	C = $\underline{O}$			
		533.6	$\underline{O}$-C			
N 1s	397.5		$\underline{N}$-Mn	**N**	3.1	
	399.5		Pyridinic (399.3) +Pyrrolic (399.9)			
	400.8		Quaternary N			
Mn $2p_{3/2}$	641.0		Mn(II)	**Mn**	5.9	12.2
		641.9	Mn(IV)			
	642.9	643.7	Mixture of Mn(IV) andother Mn with higheroxidation states			
	646.8	646.7	Satellites			
S $2p_{3/2}$	161.0	161.1	S^{2-} (MnS)	**S**	4.6	5.1
S $2p_{1/2}$	162.2	162.3				
S $2p_{3/2}$	163.4	164.2	$\underline{S}SO_3^{2-}$ (thiosulfonate)			
S $2p_{1/2}$	164.6	165.4				
S $2p_{3/2}$	168.2	168.8	$\underline{S}O_3^{2-}$ (sulfonate)and $\underline{S}O_4^{2-}$ (sulphate)			
S $2p_{1/2}$	169.4	170.0				
Atomic ratios						
			NGMS		**MnS* (reference)**	
C/Mn			11.5		3.4	
S/Mn			0.8		0.4	

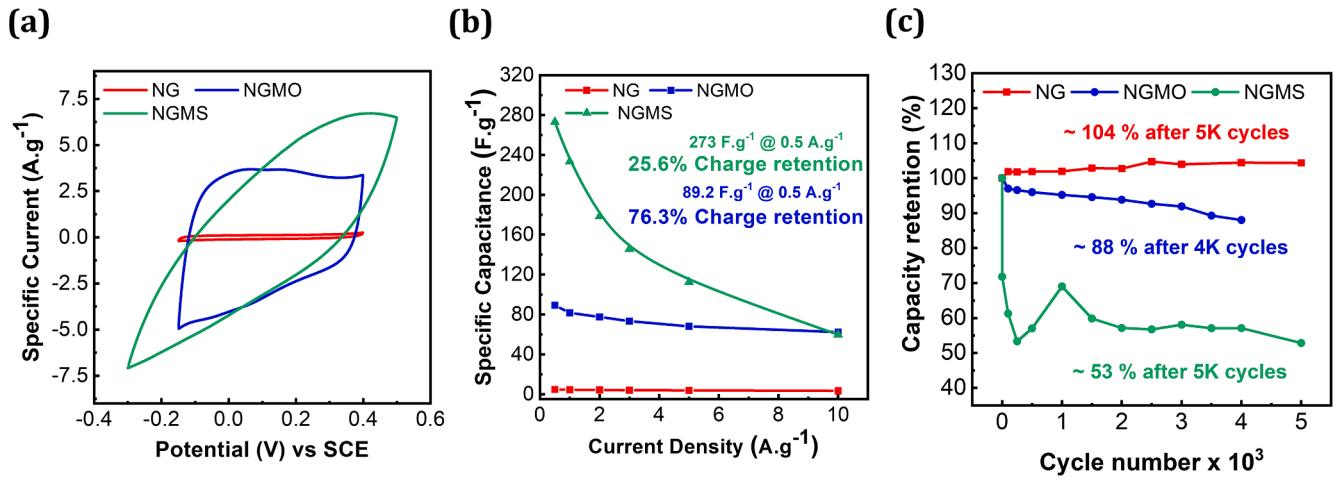

Fig. 7. The electrochemical response of the as-prepared N-doped graphene, and metal-based hybrids, namely NGMO, and NGMS, in 1 M KOH aqueous electrolyte. (a) Cyclic voltammetry at 50 mV.s^{-1}, (b) Evolution of specific capacitance at various current densities. N-graphene (NG), i.e., simple nitrogen-doped graphene is used as reference. (c) Long term stability test for NG, NGMO and NGMS samples, capacitance retention after 4 k and 5 k cycles.

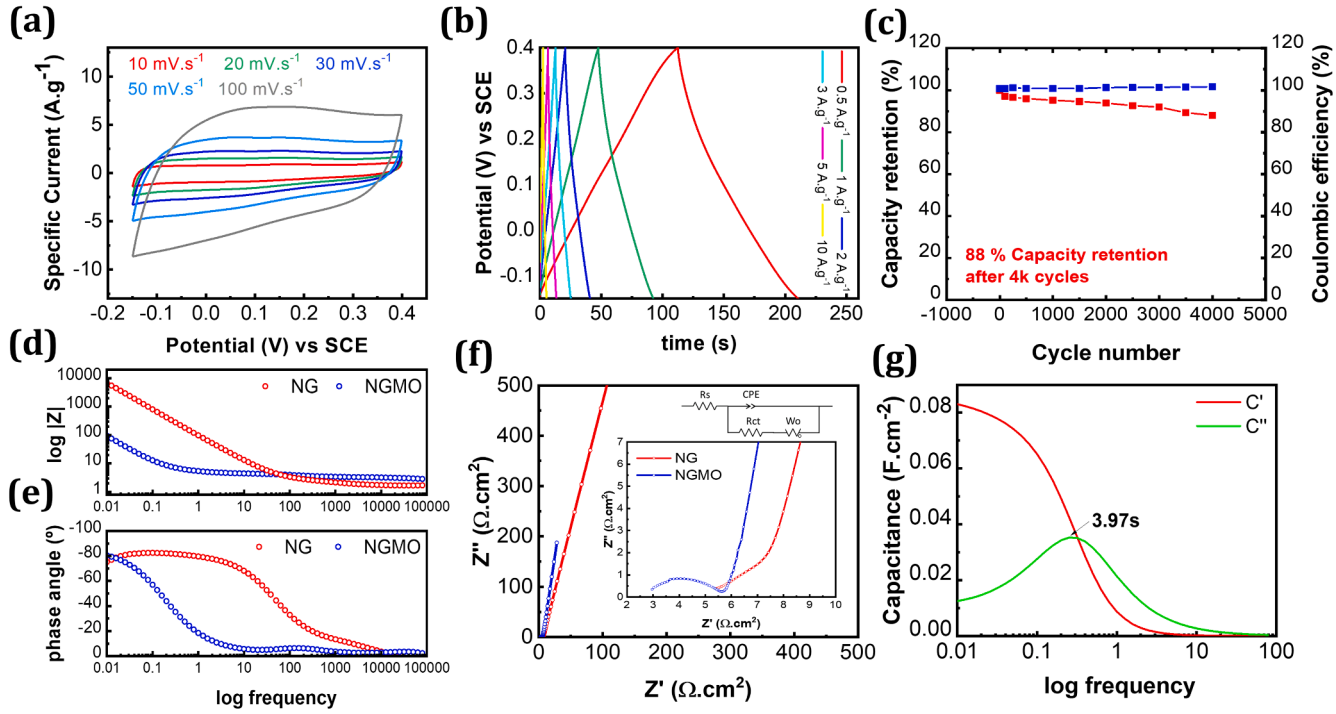

Fig. 8. Electrochemical charge storage response of the as prepared NGMO hybrids in 1 M KOH aqueous electrolyte. (a) Cyclic voltammetry performed at various scan rates, (b) Galvanic charge discharge at various charge densities, (d) Bode plot of |Z| vs. frequency, (e) Bode plot phase angle vs. frequency, (f) Nyquist plot and proposed circuit model (f) Real vs. imaginary capacitance plot, (g) Long term stability test for NGMO sample, capacitance retention and coulombic efficiency after 4000 cycles.

pseudocapacitive nature of the NGMO significantly improves the specific capacitance values reaching 89.2 F.g^{-1} at 0.5 A.g^{-1} and 81.6 F.g^{-1} at 1 A.g^{-1} in respect to N-graphene. The long-term stability test of NGMO displayed an excellent capacitance retention of 88% after 4000 GCD cycles performed at 10 A.g^{-1} (Fig. 8**c**), with a coulombic efficiency of approximately 100%.

Electrochemical Impedance Spectroscopy (EIS) were performed at OCP for better understanding the charge storage mechanism of the reference NG and NGMO hybrids. Analysis was done via the Bode plots (Fig. 8**d**–**e**) and the Nyquist plot (Fig. 8**f**). The NG spectra reveal, as expected, a capacitive slope, with a phase angle close to −80° in the medium to low-frequency range. The presence of Mn oxides in the NGMO hybrids shifts the capacitive slope towards lower frequencies; however, the phase angle value is kept around −80°. This indicates that the presence of Mn oxides increases the time constant of the system, confirming that the material response is governed by a fast faradic process, *i.e.*, a pseudocapacitive mechanism, and not by a faster electrochemical double layer process as observed for NG [51]. The NGMO pseudocapacitance is also evidenced through the increase of the charge transfer resistance (Rct), which is visible in the high frequency capacitive loop and that reaches approximately 3 Ohm.cm^2. This characteristic behavior has been related to the charge transfer resistance that arises in the interface region formed between the rough active manganese oxide hybrid nanostructure and the porous carbon paper substrate [52]. In the

NG, the faradic processes occur at much lower extent, due to heteroatom doping (−N or −O) **Fig. S4** with a much smaller the charge transfer resistance [53].

The supercapacitor factor of merit [38], i.e., the dielectric relaxation time, is given by $t = 1/f_o$ and represents the minimum time needed to discharge all the energy of the device with an efficiency higher than 50%. The variation of C" (ω) vs. frequency displays a relaxation time of 3.97 s, higher than the 100 ms obtained for the reference N-graphene sample. This increase is related to the faradaic nature of the charge storage mechanism of the manganese hybrids, performed on a longer time scale than the electric double layer storage mechanism of pure N-graphene [54].

EIS spectroscopy confirms the pseudocapacitive nature of the manganese hybrids that enhances the electrochemical response compared to the NG matrix. The insertion of the pseudocapacitive material induces some important changes in the charge storage response of the NG material, namely higher specific capacitance is obtained at the cost of a higher frequency (faster) response. Moreover, NGMO performs very well after a long-term stability test, retaining 88% of specific capacitance after 4000 cycles.

4. Conclusions

A novel microwave plasmas-based method has been applied to fabricate hybrid N-graphene (nitrogen-doped graphene)-metal-based nanostructures bearing potential for multiple applications. The synthesis was accomplished using methane/methylamine as carbon and nitrogen precursors and MnO_2 and oxy-MnS micron size particles. Synthesis of hybrid nanostructures comprising N-graphene (4.6 *at. N %*), decorated with nano-sized (~10–30 nm) manganese oxides was accomplished. Besides, hybrid N-graphene-metal sulfide nanostructures were fabricated, having MnS, MnO, $MnSO_4$ and $MnSO_3$ nanoparticles anchored to N-graphene sheets (3.1 *at. N%*).

The electrochemical charge storage properties of the developed NG, NGMO and NGMS materials were studied. The NGMO material shows average specific capacitance values, of 89.2 $F.g^{-1}$ @ 0.5 $A.g^{-1}$, very good charge retention value of 76.3%, and excellent specific capacitance retention (88%) after 4000 cycles.

Application of the presented technique to produce graphene-metal-based hybrid nanostructures at a high-yield, can potentially reduce the use of harsh chemistry. The use of a high energy density plasma environment as a tool to control the energy and particles fluxes in the assembly zone of the reactor is the main advantage in respect to conventional methods. By leveraging the unique plasma ability to control the energy and matter fluxes at the atomic scale, effective control over the whole assembly process at nanoscales can be achieved. Moreover, the method is versatile since a single plasma reactor can be used to produce hybrid nanostructures with different compositions, morphologies and architectures by simply choosing the starting materials and tailoring the plasma environment. The microwave plasma driven synthesis is controllable at a single step and atmospheric pressure conditions, allows continuous production in an environmentally friendly manner. Hundreds of milligrams of ready for use free-standing hybrids can be fabricated in minutes. Further fine-tuning of the manganese nanoparticles morphology will enable a considerable advance in the electrochemical charge storage properties of the active material. The method can be considered as a competitive alternative of chemical approaches and sustainable strategy to synthesize disruptive complex nanostructures.

Declaration of Competing Interest

The authors declare that they have no known competing financial interests or personal relationships that could have appeared to influence the work reported in this paper.

Acknowledgements

This work was performed under the framework of the PEGASUS (Plasma Enabled and Graphene Allowed Synthesis of Unique nano-Structures) project, funded by the European Union's Horizon research and innovation program under grant agreement No 766894. Work partially funded by Portuguese FCT - Fundação para a Ciência e a Tecnologia, through Eager project (PTDC/NAN-MAT/30565/2017) and strategic projects UIDB/50010/2020 and UIDP/50010/2020. M.A. and J.K. thank the support by the European Regional Development Fund within the Operational Programme "Science and Education for Smart Growth 2014 - 2020" under the Project CoE "National center of mechatronics and clean technologies "BG05M2OP001-1.001-0008". Authors would also like to thank the Fundação para a Ciência e a Tecnologia (FCT) for support with iBB projects UIDB/04565/2020 and UIDP/04565/2020 and i4HB project LA/P/0140/2020, and Slovenian Research Agency for support through project N2-0091. F.M. Dias, J. Henriques and I. Dionisio are acknowledged for the technical assistance regarding metal particles injection system and L. Silva for the assistance regarding the hybrids XRD characterization.

Appendix A. Supplementary data

Supplementary data to this article can be found online at https://doi.org/10.1016/j.cej.2021.133153.

References

[1] Z.-S. Wu, G. Zhou, L.-C. Yin, W. Ren, F. Li, H.-M. Cheng, Graphene/metal oxide composite electrode materials for energy storage, Nano Energy 1 (1) (2012) 107–131, https://doi.org/10.1016/j.nanoen.2011.11.001.

[2] M. Beidaghi, C. Wang, Micro-supercapacitors based on interdigital electrodes of reduced graphene oxide and carbon nanotube composites with ultrahigh power handling performance, Adv. Funct. Mater. 22 (21) (2012) 4501–4510, https://doi.org/10.1002/adfm.v22.2110.1002/adfm.201201292.

[3] Y. Wang, Y. Wu, Y. Huang, F. Zhang, X. Yang, Y. Ma, Y. Chen, Preventing graphene sheets from restacking for high-capacitance performance, J Phys Chem C 115 (46) (2011) 23192–23197, https://doi.org/10.1021/jp206444e.

[4] Q. Cheng, J. Tang, J. Ma, H. Zhang, N. Shinya, L.-C. Qin, Graphene and carbon nanotube composite electrodes for supercapacitors with ultra-high energy density, Phys Chem Chem Phys 13 (2011) 17615–17624, https://doi.org/10.1039/C1CP21910C.

[5] M. Khan, M.N. Tahir, S.F. Adil, H.U. Khan, M.R.H. Siddiqui, A.A. Al-warthan, W. Tremel, Graphene based metal and metal oxide nanocomposites: synthesis, properties and their applications, J Mater Chem A 3 (37) (2015) 18753–18808, https://doi.org/10.1039/C5TA02240A.

[6] P. Geng, S. Zheng, H. Tang, R. Zhu, L.i. Zhang, S. Cao, H. Xue, H. Pang, Transition metal sulfides based on graphene for electrochemical energy storage, Adv Energy Mater 8 (15) (2018) 1703259, https://doi.org/10.1002/aenm.v8.1510.1002/aenm.201703259.

[7] M.I.A. Abdel Maksoud, R.A. Fahim, A.E. Shalan, M. Abd Elkodous, S.O. Olojede, A. I. Osman, C. Farrell, A.H. Al-Muhtaseb, A.S. Awed, A.H. Ashour, D.W. Rooney, Advanced materials and technologies for supercapacitors used in energy conversion and storage: a review, Environ. Chem. Lett. 19 (1) (2021) 375–439, https://doi.org/10.1007/s10311-020-01075-w.

[8] Y. Huang, L. Lin, T. Shi, S. Cheng, Y. Zhong, C. Chen, Z. Tang, Graphene quantum dots-induced morphological changes in CuCo2S4 nanocomposites for supercapacitor electrodes with enhanced performance, Appl. Surf. Sci. 463 (2019) 498–503, https://doi.org/10.1016/j.apsusc.2018.08.247.

[9] X. Rui, H. Tan, Q. Yan, Nanostructured metal sulfides for energy storage, Nanoscale 6 (17) (2014) 9889, https://doi.org/10.1039/C4NR03057E.

[10] H. Liu, X. Liu, S. Wang, H.-K. Liu, L. Li, Transition metal based battery-type electrodes in hybrid supercapacitors: A review, Energy Storage Mater. 28 (2020) 122–145, https://doi.org/10.1016/j.ensm.2020.03.003.

[11] R.B. Pravin, P. Ingole, Challenges and prospects of metal sulfide materials for supercapacitors, Curr. Opin. Electrochem. 21 (2020) 327–334, https://doi.org/10.1016/j.coelec.2020.03.022.

[12] Q. Lai, Y. Zhao, J. Zhu, Y. Liang, J. He, J. Chen, Directly anchoring highly dispersed copper sites on nitrogen-doped carbon for enhanced oxygen reduction electrocatalysis, Chem Electro Chem 5 (14) (2018) 1822–1826, https://doi.org/10.1002/celc.v5.1410.1002/celc.201800058.

[13] G. Yuan, J. Xiang, H. Jin, L. Wu, Y. Jin, Y. Zhao, Anchoring ZnO nanoparticles in nitrogen-doped graphene sheets as a high-performance anode material for lithium-ion batteries, Materials 11 (2018) 1, https://doi.org/10.3390/ma11010096.

[14] H. Wang, C. Jiang, C. Yuan, Q. Wu, Q. Li, Q. Duan, Complexing agent engineered strategy for anchoring SnO_2 nanoparticles on sulfur/nitrogen co-doped graphene

for superior lithium and sodium ion storage, Chem. Eng. J. 332 (2018) 237–244, https://doi.org/10.1016/j.cej.2017.09.081.
[15] H. Wang, T. Maiyalagan, X. Wang, Review on recent progress in nitrogen-doped graphene: synthesis, characterization, and its potential applications, ACS Catal 2 (5) (2012) 781–794, https://doi.org/10.1021/cs200652y.
[16] Y. Qiu, X. Zhang, S. Yang, High performance supercapacitors based on highly conductive nitrogen-doped graphene sheets, Phys Chem Chem Phys 13 (2011) 12554–12558, https://doi.org/10.1039/C1CP21148J.
[17] H.M. Jeong, J.W. Lee, W.H. Shin, Y.J. Choi, H.J. Shin, J.K. Kang, J.W. Choi, Nitrogen-doped graphene for high-performance ultracapacitors and the importance of nitrogen-doped sites at basal planes, Nano Lett 11 (6) (2011) 2472–2477, https://doi.org/10.1021/nl2009058.
[18] J. Mei, L. Zhang, Anchoring high-dispersed mno_2 nanowires on nitrogen doped graphene as electrode materials for supercapacitors, Electrochim. Acta 173 (2015) 338–344, https://doi.org/10.1016/j.electacta.2015.05.064.
[19] H.R. Naderi, P. Norouzi, M.R. Ganjali, Electrochemical study of a novel high performance supercapacitor based on MnO_2/nitrogen-doped graphene nanocomposite, Appl. Surf. Sci. 366 (2016) 552–560, https://doi.org/10.1016/j.apsusc.2016.01.058.
[20] J. Yan, Z. Fan, T. Wei, W. Qian, M. Zhang, F. Wei, Fast and reversible surface redox reaction of graphene–MnO2 composites as supercapacitor electrodes, Carbon 48 (13) (2010) 3825–3833, https://doi.org/10.1016/j.carbon.2010.06.047.
[21] C. Hu, T. Lu, F. Chen, R. Zhang, A brief review of graphene–metal oxide composites synthesis and applications in photocatalysis, J. Chin. Adv. Mater. Soc. 1 (1) (2013) 21–39, https://doi.org/10.1080/22243682.2013.771917.
[22] J. Duan, S. Chen, S. Dai, S.Z. Qiao, Shape control of mn_3o_4 nanoparticles on nitrogen-doped graphene for enhanced oxygen reduction activity, Adv Funct Mater 24 (14) (2014) 2072–2078, https://doi.org/10.1002/adfm.v24.1410.1002/adfm.201302940.
[23] Y. Ioni, E. Buslaeva, S. Gubin, Synthesis of graphene with noble metals nanoparticles on its surface, Mater. Today:. Proc. 3S (2016) S209–S213, https://doi.org/10.1016/j.matpr.2016.02.035.
[24] K. Zhang, P. Han, L. Gu, L. Zhang, Z. Liu, Q. Kong, C. Zhang, S. Dong, Z. Zhang, J. Yao, H. Xu, G. Cui, L. Chen, Synthesis of nitrogen-doped mno/graphene nanosheets hybrid material for lithium ion batteries, ACS Appl Mater Interfaces 4 (2) (2012) 658–664, https://doi.org/10.1021/am201173z.
[25] R. Chen, J. Yan, Y. Liu, J. Li, Three-dimensional nitrogen-doped graphene/mno nanoparticle hybrids as a high-performance catalyst for oxygen reduction reaction, J. Phys. Chem. C 119 (15) (2015) 8032–8037, https://doi.org/10.1021/acs.jpcc.5b00306.
[26] A. Jana, E. Scheer, S. Polarz, Synthesis of graphene–transition metal oxide hybrid nanoparticles and their application in various fields, Beilstein J Nanotechnol 8 (2017) 688–714, https://doi.org/10.3762/bjnano.8.74.
[27] Z. Li, J. Wang, S. Liu, X. Liu, S. Yang, Synthesis of hydrothermally reduced graphene/MnO_2 composites and their electrochemical properties as supercapacitors, J. Power Sources 196 (19) (2011) 8160–8165, https://doi.org/10.1016/j.jpowsour.2011.05.036.
[28] W.S. Hummers, R.E. Offeman, Preparation of graphitic oxide, J Am Chem Soc 80 (6) (1958) 1339, https://doi.org/10.1021/ja01539a017.
[29] Q. Ke, J. Wang, Graphene-based materials for supercapacitor electrodes - A review, J Materiomics 2 (1) (2016) 37–54, https://doi.org/10.1016/j.jmat.2016.01.001.
[30] E. Tatarova, A. Dias, E. Felizardo, N. Bundaleski, M. Abrashev, J. Henriques, Z. Rakočević, L.L. Alves, Atmospheric Pressure Plasmas: Processes, Technology and Applications: Microwave Plasmas Applied for Synthesis of Free-Standing Carbon Nanostructures at Atmospheric Pressure Conditions, in: M. Parker (Ed.), Nova Science Publishers, 2016. ISBN: 978-1-63485-214-2. https://novapublishers.com/shop/atmospheric-pressure-plasmas-processes-technology-and-applications/.
[31] A. Dias, E. Felizardo, D. Tsyganov, N. Bundaleska, M. Abrashev, E. Tatarova, Microwave Discharges: Fundamentals and Applications: Assembling and engineering of 2D carbon nanostructures by microwave plasmas, in: A. Gamero, A. Sola (Eds.), UCO Press. Editorial Universidad de Córdoba, 2015. ISBN: 978-84-9927-187-3. http://www.uco.es/servicios/ucopress/index.php/es/?option=com_hikashop&ctrl=product&task=show&cid=503&name=microwave-discharges-fundamentals-and-applications&Itemid=885&category_pathway=55.
[32] N. Bundaleska, D. Tsyganov, A. Dias, E. Felizardo, J. Henriques, F.M. Dias, M. Abrashev, J. Kissovski, E. Tatarova, Microwave plasmas enabled synthesis of free standing carbon nanostructures at atmospheric pressure conditions, Phys. Chem. Chem. Phys. 20 (2018) 13810–13824, https://doi.org/10.1039/c8cp01896k.
[33] A. Dias, N. Bundaleski, E. Tatarova, F.M. Dias, M. Abrashev, U. Cvelbar, O.M.N. D. Teodoro, J. Henriques, Production of N-graphene by microwave N2-Ar plasma, J Phys D: Appl. Phys. 49 (2016), 055307, https://doi.org/10.1088/0022-3727/49/5/055307 (9pp).
[34] E. Tatarova, A. Dias, J. Henriques, M. Abrashev, N. Bundaleska, E. Kovacevic, N. Bundaleski, U. Cvelbar, E. Valcheva, B. Arnaudov, A.M.B. do Rego, A. M. Ferraria, J. Berndt, E. Felizardo, O.M.N.D. Teodoro, T.h. Strunskus, L.L. Alves, B. Gonçalves, Towards large-scale in free-standing graphene and N-graphene sheets, Sci. Rep. 7 (1) (2017), https://doi.org/10.1038/s41598-017-10810-3.
[35] N. Bundaleska, A. Dias, N. Bundaleski, E. Felizardo, J. Henriques, D. Tsyganov, M. Abrashev, E. Valcheva, J. Kissovski, A.M. Ferraria, A.M.B. do Rego, A. Almeida, J. Zavašnik, U. Cvelbar, O.M.N.D. Teodoro, T.h. Strunskus, E. Tatarova, Prospects for microwave plasma synthesized N-graphene in secondary electron emission mitigation applications, Sci. Rep. 10 (1) (2020), https://doi.org/10.1038/s41598-020-69844-9.
[36] M. Moisan, Z. Zakrzewski, Plasma sources based on the propagation of electromagnetic surface waves, J Phys D: Appl Phys 24 (7) (1991) 1025–1048, https://doi.org/10.1088/0022-3727/24/7/001.
[37] D. Tsyganov, N. Bundaleska, A. Dias, J. Henriques, E. Felizardo, M. Abrashev, J. Kissovski, A.M.B. do Rego, A.M. Ferraria, E. Tatarova, Microwave plasma-based direct synthesis of free-standing N-graphene, Phys. Chem. Chem. Phys. 22 (8) (2020) 4772–4787, https://doi.org/10.1039/C9CP05509F.
[38] D. Tsyganov, N. Bundaleska, J. Henriques, E. Felizardo, A. Dias, M. Abrashev, J. Kissovski, A.M. Botelho do Rego, A.M. Ferraria, E. Tatarova, Simultaneous synthesis and nitrogen doping of free-standing graphene applying microwave plasma, Materials 13 (18) (2020;13:4213.) 4213, https://doi.org/10.3390/ma13184213.
[39] D. Tsyganov, N. Bundaleska, E. Tatarova, A. Dias, J. Henriques, A. Rego, A. Ferraria, M.V. Abrashev, F.M. Dias, C.C. Luhrs, J. Phillips, On the plasma-based growth of 'flowing' graphene sheets at atmospheric pressure conditions, J Plasma Sources Sci Technol. 25 (1) (2016) 015013, https://doi.org/10.1088/0963-0252/25/1/015013.
[40] N. Bundaleska, J. Henriques, M. Abrashev, A.M. Botelho do Rego, A.M. Ferraria, A. Almeida, F.M. Dias, E. Valcheva, B. Arnaudov, K.K. Upadhyay, M.F. Montemor, E. Tatarova, Large-scale synthesis of free-standing N-doped graphene using microwave plasma, Sci. Rep. 8 (1) (2018), https://doi.org/10.1038/s41598-018-30870-3.
[41] I.L. Knuniantc (Ed.), Chemical encyclopedia, Russian Encyclopedia Edition, Moscow, 1992.
[42] D. Tsyganov, N. Bundaleska, E. Tatarova, C.M. Ferreira, Ethanol reforming into hydrogen-rich gas applying microwave 'tornado'-type plasma, Int J Hydrogen Energy 38 (34) (2013) 14512–14530, https://doi.org/10.1016/j.ijhydene.2013.08.127.
[43] J.-B. Wu, M.-L. Lin, X. Cong, H.-N. Liu, P.-H. Tan, Raman spectroscopy of graphene-based materials and its applications in related devices, Chem Soc Rev 47 (5) (2018) 1822–1873, https://doi.org/10.1039/C6CS00915H.
[44] L. Malavasi, P. Galinetto, M.C. Mozzati, C.B. Azzonib, G. Flora, Raman spectroscopy of AMn_2O_4 (A = Mn, Mg and Zn) spinels, Phys. Chem. Chem. Phys. 4 (15) (2002) 3876–3880, https://doi.org/10.1039/b203520k.
[45] L. Yang, S. Cheng, X.u. Ji, Y.u. Jiang, J. Zhou, M. Liu, Investigations into the origin of pseudocapacitive behavior of Mn_3O_4 electrodes using in operando Raman spectroscopy, J Mater Chem A 3 (14) (2015) 7338–7344, https://doi.org/10.1039/C5TA00223K.
[46] G. Beamson, D. Briggs, High resolution XPS of organic polymers The Scienta ESCA300 Database, John Wiley (1992).
[47] NIST X-ray Photoelectron Spectroscopy Database. NIST Standard Reference Database 20, Version 4.1. Data compiled and evaluated by Alexander V. Naumkin, Anna Kraut-Vass, Stephen W. Gaarenstroom, and Cedric J. Powell, 2012. Available online: https://srdata.nist.gov/xps/. http://dx.doi.org/10.18434/T4T88K.
[48] M.C. Biesinger, B.P. Payne, A.P. Grosvenor, L.W.M. Lau, A.R. Gerson, R.S.C. Smart, Resolving surface chemical states in XPS analysis of first row transition metals, oxides and hydroxides: Cr, Mn, Fe Co and Ni, App. Surface Sci. 257 (7) (2011) 2717–2730, https://doi.org/10.1016/j.apsusc.2010.10.051.
[49] R.P. Gandhiraman, D. Nordlund, C. Javier, J.E. Koehne, B. Chen, M. Meyyappan, X-ray absorption study of graphene oxide and transition metal oxide nanocomposites, J Phys Chem C 118 (32) (2014) 18706–18712, https://doi.org/10.1021/jp503941t.
[50] Y. Su, H. Chai, Z. Sun, T. Liu, D. Jia, W. Zhou, High-performance manganese nanoparticles on reduced graphene oxide for oxygen reduction reaction, Catal. Lett. 146 (6) (2016) 1019–1026, https://doi.org/10.1007/s10562-016-1719-4.
[51] B.E. Conway, W.G. Pell, Double-layer and pseudocapacitance types of electrochemical capacitors and their applications to the development of hybrid devices, J Solid State Electrochem 7 (9) (2003) 637–644, https://doi.org/10.1007/s10008-003-0395-7.
[52] A. Allison, H.A. Andreas, Minimizing the nyquist-plot semi-circle of pseudocapacitive manganese oxides through modification of the oxide-substrate interface resistance, J Power Sources 426 (2019) 93–96, https://doi.org/10.1016/j.jpowsour.2019.04.029.
[53] D. Yang, Y.u. Song, Y.-J. Ye, M. Zhang, X. Sun, X.-X. Liu, Boosting the pseudocapacitance of nitrogen-rich carbon nanorod arrays for electrochemical capacitors, J. Mater. Chem. A 7 (19) (2019) 12086–12094, https://doi.org/10.1039/C9TA01973A.
[54] R.R. Salunkhe, Y.-H. Lee, K.-H. Chang, J.-M. Li, P. Simon, J. Tang, N.L. Torad, C.-C. Hu, Y. Yamauchi, Nanoarchitectured graphene-based supercapacitors for next-generation energy-storage applications, Chem Eur J 20 (43) (2014) 13838–13852, https://doi.org/10.1002/chem.v20.4310.1002/chem.201403649.